Nanoscale

PAPER

View Article Online
View Journal | View Issue

Cite this: *Nanoscale*, 2017, **9**, 7501

Phase transition and *in situ* construction of lateral heterostructure of 2D superconducting α/β Mo_2C with sharp interface by electron beam irradiation†

Zhibo Liu,‡[a] Zeyuan Fei,‡[a,b] Chuan Xu,[a] Yixiao Jiang,[a] Xiu-Liang Ma,*[a] Hui-Ming Cheng[a] and Wencai Ren *[a]

Received 6th March 2017,
Accepted 30th April 2017

DOI: 10.1039/c7nr01609c

rsc.li/nanoscale

Lateral heterostructures of 2D materials have several interesting properties and potential applications, and they are usually fabricated by chemical vapor deposition. However, it still remains a great challenge to fabricate 2D lateral heterostructures with well-controlled patterns and sharp interfaces. Herein, we found that the 2D α-Mo_2C crystal, a recently emerging 2D superconductor, experiences a phase transition from the α phase to β phase on electron beam irradiation in a transmission electron microscope because of the migration of carbon atoms among the molybdenum octahedrons. Combined with first-principles calculations, the carbon atom migration paths and the corresponding energy barriers were discussed. Utilizing this unique phase transition property of 2D α-Mo_2C crystal, we demonstrated the precise *in situ* construction of the lateral heterostructure of 2D superconducting α/β Mo_2C with a well-controlled pattern and sharp interface using advanced aberration-corrected scanning transmission electron microscopy.

Introduction

Abundant two-dimensional (2D) atomic crystals with a variety of properties provide a platform that allows the creation of 2D vertical and lateral heterostructures with numerous interesting properties and potential electronic and optoelectronic applications.[1–12] Currently, several 2D lateral heterostructures such as graphene/h-BN and MoS_2/WSe_2 have been fabricated by chemical vapor deposition (CVD).[2,3,7,12] However, it is very difficult to fabricate heterostructures with well-controlled patterns and sharp interfaces. Alternatively, *in situ* electron beam irradiation provides a precise way to fabricate 2D lateral heterostructures,[13–19] which utilizes phase transition or local modification of 2D materials under electron beam irradiation. For example, the H → T phase transition of MoS_2 under electron irradiation leads to the fabrication of the monolayer semiconductor–conductor 2D lateral heterostructure.[19] However, the T-phase MoS_2 is unstable,[20] and it can be easily destroyed by electron beam irradiation.[17,18]

Ultrathin transition metal carbides (TMCs) and MXenes are an emerging class of novel 2D materials with several fascinating properties and promising applications.[21–27] For example, CVD-grown high-quality ultrathin Mo_2C crystals have been demonstrated to be a very stable and clean 2D superconductor system,[21–23] and MXenes have potential applications in electrochemical energy storage, catalysis, and thermoelectric energy conversion.[24–27] Similar to MoS_2, very interestingly, Mo_2C has two different phases, *i.e.* orthorhombic (α) and hexagonal (β) phases, depending on the different distribution of interstitial carbon atoms in the Mo matrix.[22,28,29] They have been shown or theoretically predicted to have different properties such as superconducting transition temperature (T_C) and catalytic activity.[30–34] This opens up the possibility for constructing lateral heterostructures of 2D superconducting α/β Mo_2C.

It is known that vortex matter in mesoscopic superconductors is strongly affected by the geometry of the sample.[35,36] In the lateral heterostructures of 2D superconducting α/β Mo_2C, the strong geometrical confinement at the interfacial regions could impose a potential barrier for the vortex transverse motion, forming an effective one-dimensional wire for vortex matter. This can provide a promising platform for studying vortex physics at the nanoscale. In addition, it has been widely demonstrated that the heterostructures of different catalysts have much higher catalytic activity than individual ones because of the synergistically enhanced activity at the interface. For example, the heterostructures of MoC–Mo_2C and Fe_3C–Mo_2C remarkably improve the hydrogen evolution reac-

[a]*Shenyang National Laboratory for Materials Science, Institute of Metal Research, Chinese Academy of Sciences, Shenyang 110016, P. R. China.*
E-mail: wcren@imr.ac.cn, xlma@imr.ac.cn
[b]*School of Materials Science and Engineering, University of Science and Technology of China, Hefei 230026, P. R. China*

†Electronic supplementary information (ESI) available. See DOI: 10.1039/c7nr01609c

‡These authors contributed equally to this work.

tion.[37,38] Therefore, our lateral heterostructure of α/β Mo_2C also provides a platform to investigate the synergistic effects between α and β phases at the interface, which are likely to improve the catalytic activities in some reactions. However, how to fabricate this heterostructure in a well-controlled manner and with a sharp interface is still unknown.

Herein, we found that electron beam irradiation can induce phase transition from the α phase to β phase in a 2D α-Mo_2C crystal, as observed using transmission electron microscopy (TEM), because of the migration of carbon atoms among the molybdenum octahedrons. The carbon migration paths and the corresponding energy barriers were discussed based on first-principles calculations. Utilizing this unique phase transition property of 2D α-Mo_2C crystal, we demonstrated the precise *in situ* construction of the lateral heterostructure of the 2D superconducting α/β Mo_2C with a well-controlled pattern and sharp interface with the help of advanced aberration-corrected scanning transmission electron microscope (STEM).

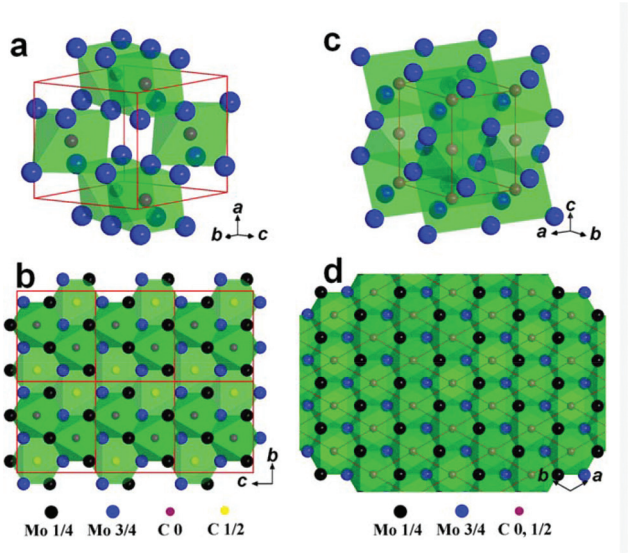

Fig. 1 Schematic of crystalline structure of α-Mo_2C and β-Mo_2C. (a, c) Unit cells of α-Mo_2C (a) and β-Mo_2C (c). (b, d) Projections along the [100] direction of α-Mo_2C (b) and [0001] direction of β-Mo_2C (d).

Experimental details

The 2D α-Mo_2C crystals were synthesized by CVD on a Cu/Mo substrate and transferred to the TEM grid by etching away the Cu in $(NH_4)_2S_2O_8$ solution, as reported in our previous study.[21] The thicknesses of the crystals are less than 10 nm (Fig. S1†). FEI Tecnai T12 working at 120 kV accelerating voltage was used to collect the selected area electron diffraction (SAED) patterns. High-angle angular dark-field (HAADF)-STEM measurements were conducted on a 300 kV FEI Titan G2 60–300 equipped with a high-brightness field-emission gun (X-FEG), double spherical aberration correctors and a monochromator. Vienna *ab initio* simulation package (VASP) within the density functional theory (DFT) was used to perform the first-principles calculations. The Perdew–Burke–Ernzerhof form of the generalized gradient approximation (GGA) was used as the exchange–correlation functional. Mo $4p^6 4d^5 5s^1$ and C $2s^2 2p^2$ served as the valence states using the projector augmented wave (PAW) pseudopotentials with an energy cutoff of 500 eV. For the 2 × 2 × 2 one-carbon-atom-migrated supercell, the Brillouin zone was sampled with a 3 × 3 × 3 Monkhorst–Pack *k*-point mesh. The structural optimization was performed through the conjugate-gradient (CG) method until the Hellmann–Feynman force on each atom was less than 5 meV $Å^{-1}$.

Results and discussion

As shown in Fig. 1a and b, α-Mo_2C is composed of hexagonal closely packed (HCP) molybdenum atoms and octahedral-interstitial carbon atoms that present an ordered zigzag configuration in every layer perpendicular to the lattice vector ***b***-axis direction. Because of the off-center deviation of the carbon atoms in the octahedrons, the sublattice of Mo atoms is, consequently, slightly distorted.[22,39] β-Mo_2C is a disordered high-temperature counterpart of ordered room-temperature phase α-Mo_2C.[39] Different from α-Mo_2C, β-Mo_2C comprises rigorous HCP Mo atoms with octahedral centers randomly occupied by interstitial carbon atoms (Fig. 1c). It is noted that the theoretical probability for the occupation of carbon atoms at the octahedral sites is 50%.[39,40] However, the projections along the [100] zone axis of α-Mo_2C and [0001] zone axis of β-Mo_2C have indistinguishable atomic configurations (Fig. 1b and d).

Fig. 2a shows a bright-field (BF) TEM image of an octagonal 2D α-Mo_2C crystal, and Fig. 2b shows a SAED pattern that was taken from a circular area of ~1.2 μm in diameter in Fig. 2a. Superlattice diffraction spots denoted by red arrows are observed in Fig. 2b. Fig. 2d and e show the simulated ED patterns of α- and β-Mo_2C, respectively. It can be found that the only difference between the orthorhombic phase and hexagonal phase lies in whether the superlattice diffraction spots enclosed by the red circles exist or not. The (040) and (002) ED spots of α-Mo_2C could be correspondingly indexed as the $(1\bar{2}10)$ and $(10\bar{1}0)$ ED spots of β-Mo_2C after phase transition. In α-Mo_2C, the carbon atoms are distributed orderly and attract each other in the Mo octahedrons, leading to a regular distortion of the HCP lattice. However, there is no Mo lattice distortion in the β phase because of the disordered and random distribution of carbon atoms, which mutually offset the interaction. Therefore, the α phase generates superlattice diffraction spots in the ED patterns, but the β phase does not. It is important to note that the orthorhombic characteristic ED spots (superlattice diffraction spots) disappear after irradiation for about 30 min with a beam current density of ~4.2 A cm^{-2}, as shown in Fig. 2c, indicating that the order–disorder transition from α-Mo_2C to β-Mo_2C occurs. Fig. 2f shows the intensity evolution of the superlattice diffraction spot (020) against

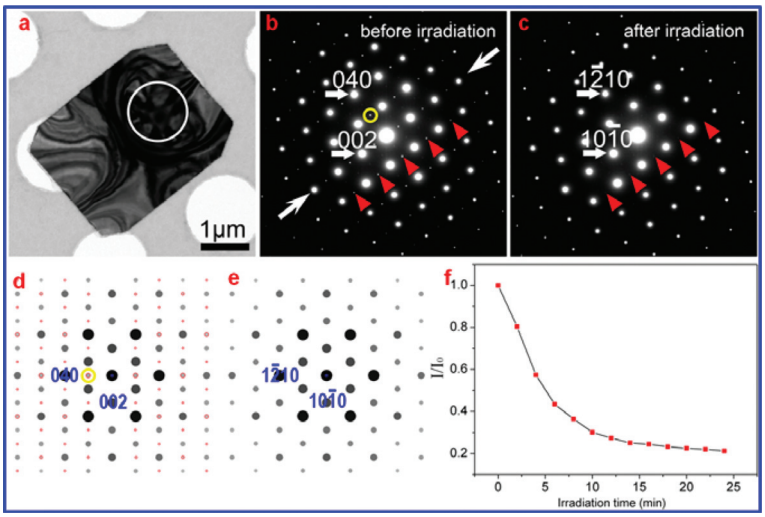

Fig. 2 (a) BF-TEM image of an octagonal 2D α-Mo_2C crystal. (b, c) SAED patterns obtained from the area marked by a circle in (a) before irradiation and (b) after irradiation (c). (d, e) Simulated electron diffraction pattern of α-Mo_2C (d) and β-Mo_2C (e). Superlattice diffraction spots are enclosed by red circles in (d). (f) Evolution of the intensity of superlattice diffraction spot (020) against irradiation time. The spots enclosed by yellow circles in (b) and (d) are the characteristic (020) spots.

irradiation time with a beam current density of ~3.3 A cm^{-2} in another sample, which is used to evaluate the dynamic process. The dramatic decrease in the intensity in the first 8 min implies the rapid order–disorder transition. As the irradiation proceeds, the transition slows down due to the continuous decrease in the concentration of the ordered carbon vacancies.

We also investigated the influence of electron beam irradiation on the domain boundaries of regular multi-domain 2D α-Mo_2C crystals. Fig. 3a shows a TEM image of a hexagonal 2D α-Mo_2C crystal, which is composed of six regular triangular domains (labelled as ①–⑥) with rotational symmetry and well-defined line-shaped domain boundaries, as reported in our previous study.[22] Area ③ was subjected to electron beam irradiation for 40 min. Fig. 3b shows the SAED pattern obtained from area ⑦ in Fig. 3a. The dark-field (DF) images in Fig. 3c–e were produced by selecting the domain-related (020) superlattice diffraction spots (labelled as I, II, and III in Fig. 3b). It is worth noting that all the areas except for ③ present regular triangular domains in the DF images, and the original line-shaped domain boundaries of area ③ assigned by yellow arrows in Fig. 3d disappear because of the order–disorder transition (α → β) induced by electron beam irradiation for 40 min.

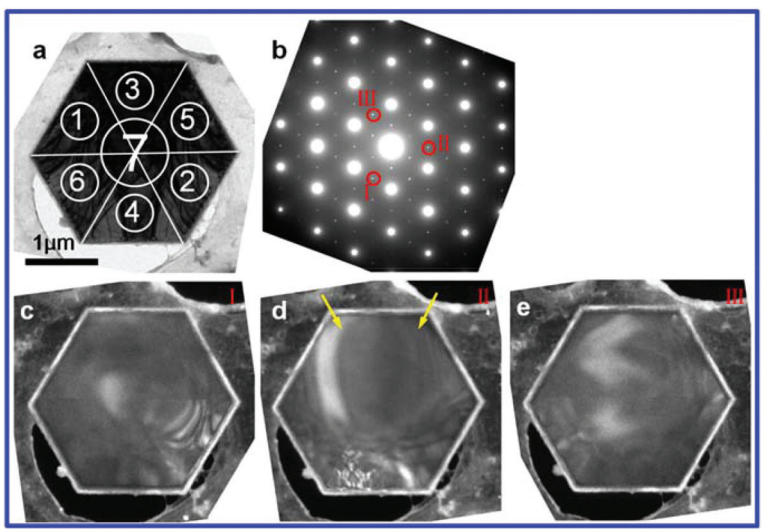

Fig. 3 (a) BF-TEM image of a hexagonal multi-domain 2D α-Mo_2C crystal. The domain boundaries are indicated by straight lines, and the domains are labelled by ①–⑥. Area ⑦ is the center of the crystal. (b) SAED pattern obtained from area ⑦ in (a). (c, d, e) DF-TEM images produced by selecting the domain-related (020) type ED spots I, II, and III in (b), respectively.

It is noted that α-Mo_2C and β-Mo_2C are closely crystallographically related, namely, $a_\alpha = c_\beta,\ \sqrt{3}b_\alpha = 2c_\alpha, b_\alpha = 2a_\beta$,[29,39] which is the basis of the order–disorder phase transition. During the order–disorder phase transition process, carbon atoms migrate among the molybdenum octahedrons by breaking the original ordered zigzag configuration and redistribute randomly in the molybdenum octahedrons with a theoretical occupation probability of 50%. Consequently, the original distorted HCP Mo sublattice relaxes to rigorous HCP configuration along with the formation of hexagonal β-Mo_2C. As shown below, the tiny atomic displacement of the Mo sublattice can be detected by aberration-corrected STEM. Due to the 2D nature, the ultrathin α-Mo_2C crystal is likely to lose carbon atoms from the surface during electron beam irradiation. Since the relationship of lattice parameters in the two phases is not changed (Fig. 2b and c), we propose that the lost carbon atoms are of small quantity compared to the carbon atoms in the lattice. Consequently, the chemical formula of 2D Mo_2C after electron beam irradiation can be written as Mo_2C_{1-x}, where x is a small number far less than 1.

As shown in Fig. 4a, every carbon atom in α-Mo_2C lattice has six neighboring octahedral vacancies. To reveal the energetic features of the order–disorder phase transition, eight main migration paths proposed for every carbon atom were analyzed. Fig. 4a shows a layer of octahedrons occupied and unoccupied by carbon atoms in the view of the [100] projective direction. There are two equivalent O_1-type octahedral vacancies (that are not shown in Fig. 4a) parallel to the lattice vector ***a***-axis direction. A carbon atom must push through the center of three planar molybdenum atoms labeled by the numbers 1, 4, and 7 in Fig. 4a, which comprise one surface of an octahedron. Since the carbon atoms are present in a zigzag configuration and are off-center in the octahedrons for α-Mo_2C (Fig. 1b), O_2-, O_3-, and O_4-type vacancies are not equivalent in terms of the same carbon atom. However, the migration paths of the carbon atom are somewhat similar for the three types of vacancies mentioned above. Herein, only O_2 is analyzed for brevity. There are two migration paths marked by the black straight line and blue broken line, as shown in Fig. 4a. For the straight line migration path, the carbon atom must push through the center of number 6 and number 7 molybdenum atoms, which comprise one ridge of the octahedron. However, for the broken line migration path, the carbon atom must first push through the co-surface (composed of numbers 4, 6, and 7 molybdenum atoms) of the octahedron and the tetrahedron composed of numbers 4, 6, 7, and 8 molybdenum atoms; second, it has to proceed toward the center of the tetrahedron. Third, it must push through another surface (composed of numbers 6, 7, and 8 molybdenum atoms) of the tetrahedron; finally, it reaches the site of the O_2-type vacancy. The migration paths of the O_3- and O_4-type vacancies are similar to those of the O_2-type vacancy in addition to the existing two broken line paths for the O_4-type vacancies in the light of symmetry.

Fig. 4b schematically illustrates the carbon atom migration processes, where the purple balls represent molybdenum atoms interacting most strongly with the migrated carbon atom, and the red balls superimposed on the solid black circles denote the original sites of carbon atoms before migration in the α-Mo_2C lattice. Fig. 4c is the system energy corresponding to every migration local site of the carbon atom in Fig. 4b. For simplicity, only the molybdenum atoms neighboring to the migrated carbon were relaxed, while the other atoms were fixed when relaxing the images of the transition paths, which avoid the migrated carbon in the transition path shifting to the neighboring octahedral or tetrahedral void during the relaxation period. We regard the energy difference between the maximum and original value as the energy barrier in each migration path. Table 1 shows the energy barriers of eight migration paths. Clearly, migration path I, which is parallel to the incident electron beam direction, has the minimal energy barrier. It is, consequently, proposed that the probability of migration path I is maximal. Because the carbon atoms with a zigzag configuration attract each other,[22] the off-center direction of the carbon atom shown in Fig. 4a is along the O_2 vacancy direction, and the carbon atom must overcome the attraction originating from the neighboring carbon atoms in the same layer to reach the O_3 vacancy. As a result, migration path IV has the maximal energy barrier. Moreover, we also find that the broken line migration paths have smaller energy barriers than straight line migration paths. Generally, the migration paths that carbon atoms push through the surface composed of three molybdenum atoms can occur easily compared to those carbon atoms that have to push through the center of two molybdenum atoms. It is noted that the maximal energy that an electron accelerated by 120 kV transmits to the carbon atom is 24.51 eV.[41,42] It is large enough to drive a carbon atom to migrate along any migration path mentioned above just with a different migration possibility. However, based on the ED and subsequent atomic-scale HAADF-STEM results, the Mo atom is stable enough in the lattice and cannot be driven to other sites by electron beam irradiation. Therefore, the order–disorder transition is indeed related to the carbon atom migration in the Mo sublattice.

Advanced aberration-corrected STEM with atomic-scale electron beam probe not only allows the detection of little atomic displacement of the Mo sublattice during phase transitions but also provides an ideal tool to precisely *in situ* construct the lateral heterostructure of 2D superconducting α/β Mo_2C with a well-controlled pattern and sharp interface. Fig. 5a shows a high-resolution HAADF-STEM image of a 2D α-Mo_2C crystal in the view of the [100] direction, where area I with a designed pattern was subjected to higher beam current density irradiation than area II. The inset in Fig. 5a is the corresponding fast Fourier transform (FFT) of the HAADF-STEM image. Fig. 5b demonstrates the inverse FFT image produced with the (020) twin spots marked by red circles in the inset of Fig. 5a. Similar to the diffraction contrast DF imaging theory, the area that produces the selected FFT spots is bright in the inverse FFT image. Therefore, area II retains the original α phase, while the α phase transforms to β phase in area I. This leads to the formation of a lateral heterostructure of 2D superconducting α/β Mo_2C with a sharp

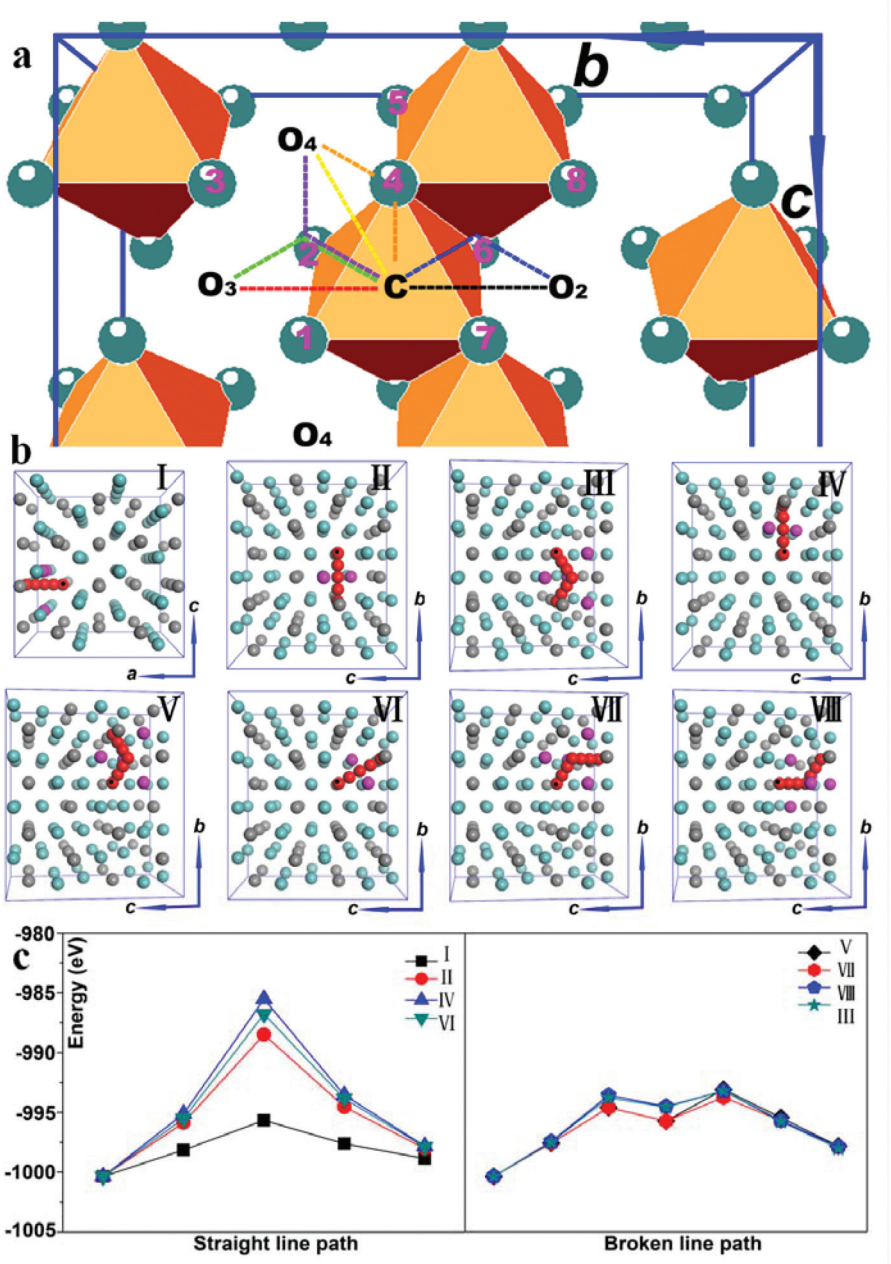

Fig. 4 Schematic of the carbon atom migration and the corresponding system energy with the migrated carbon atom stopping at the local sites in the α-Mo_2C lattice. (a) Migration paths of a carbon atom in the α-Mo_2C lattice marked by dashed lines. (b) Local sites of the migrated carbon atom. (c) System energy corresponding to the migrated carbon atom stopping at the local sites in the α-Mo_2C lattice.

Table 1 Energy barriers of eight migration paths of the carbon atom in α-Mo_2C lattice

Straight line migration paths (eV)				Broken line migration paths (eV)			
I (O_1)	II (O_2)	IV (O_3)	VI (O_4)	V (O_3)	VII (O_4)	VIII (O_4)	III (O_2)
4.703	11.899	14.847	13.593	7.296	6.631	7.166	7.175

interface of a few atoms width. Moreover, the transition areas irradiated by the electron beam are quite stable. No structural change was found even after storing under ambient conditions for a few weeks.

It is known that vortex matter in mesoscopic superconductors is strongly affected by the geometry of the sample.[35,36] Since the observed phase boundaries in our crystals are very sharp with a width of a few atoms, quantum confinement will become important and might lead to spatial modulation of the superconducting order parameter across the interface of

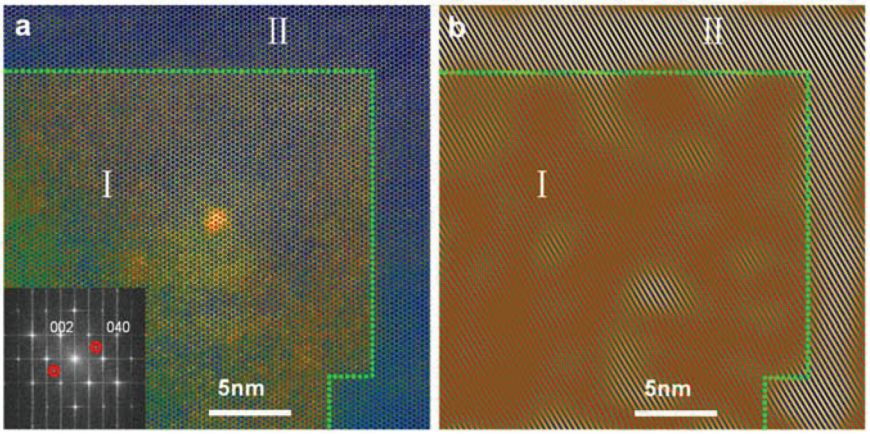

Fig. 5 (a) Atomic-scale STEM-HAADF image of a 2D α-Mo_2C crystal. Inset is the FFT. (b) Inverse FFT image of (a). The area enclosed by the green dashed line has undergone electron beam irradiation.

crystals, inducing a nanoscale inhomogeneous superconducting phase. As a result, for instance, when the superconducting state in such interfacial structures is under an applied magnetic field, it is likely that the vortices could be first nucleated near the interfacial regions. The strong geometrical confinement near the interfacial regions could impose a potential barrier for the vortex transverse motion, forming an effective one-dimensional wire for vortex matter. This provides a promising platform for studying vortex physics at the nanoscale. In addition, this lateral heterostructure also provides a platform to investigate the synergistic effects between the α and β phases at the interface, which are likely to improve the catalytic activities in some reactions. Furthermore, we can also obtain 2D β-Mo_2C crystals with exactly the same morphology and thickness with the original 2D α-Mo_2C crystals by electron beam irradiation, which can be used to investigate the intrinsic differences in the superconducting transition temperature and catalytic activity for various reactions between these two phases of Mo_2C crystals.

Conclusions

We investigated the microstructure change of 2D α-Mo_2C crystals under *in situ* electron beam irradiation in TEM. It was found that electron beam irradiation can induce phase transition from α phase to β phase in a 2D α-Mo_2C crystal, where the carbon atoms migrate from a zigzag configuration to random occupation, and the distorted HCP configuration of molybdenum atoms relaxes to a rigorous HCP configuration. The first-principles calculations show that carbon atom migration parallel to the incident electron beam direction has the minimal energy barrier. Utilizing this unique phase transition property of 2D α-Mo_2C crystal, the lateral heterostructures of 2D superconducting α/β Mo_2C with a well-controlled pattern and sharp interface were fabricated using advanced aberration-corrected STEM.

Acknowledgements

The authors thank Drs N. Kang and D.H. Deng for valuable discussions. This study was supported by the National Science Foundation of China (no. 51325205, 51290273, and 51521091), and the Chinese Academy of Sciences (no. KGZD-EW-303-1, and KGZD-EW-T06).

References

1 W. Yang, G. Chen, Z. Shi, C. C. Liu, L. Zhang, G. Xie, M. Cheng, D. Wang, R. Yang, D. Shi, K. Watanabe, T. Taniguchi, Y. Yao, Y. Zhang and G. Zhang, *Nat. Mater.*, 2013, **12**, 792–797.
2 Z. Liu, L. Ma, G. Shi, W. Zhou, Y. Gong, S. Lei, X. Yang, J. Zhang, J. Yu, K. P. Hackenberg, A. Babakhani, J. C. Idrobo, R. Vajtai, J. Lou and P. M. Ajayan, *Nat. Nanotechnol.*, 2013, **8**, 119–124.
3 M. P. Levendorf, C. J. Kim, L. Brown, P. Y. Huang, R. W. Havener, D. A. Muller and J. Park, *Nature*, 2012, **488**, 627–632.
4 T. Gao, X. J. Song, H. W. Du, Y. F. Nie, Y. B. Chen, Q. Q. Ji, J. Y. Sun, Y. L. Yang, Y. F. Zhang and Z. F. Liu, *Nat. Commun.*, 2015, **6**, 6835.
5 T. Georgiou, R. Jalil, B. D. Belle, L. Britnell, R. V. Gorbachev, S. V. Morozov, Y. J. Kim, A. Gholinia, S. J. Haigh, O. Makarovsky, L. Eaves, L. A. Ponomarenko, A. K. Geim, K. S. Novoselov and A. Mishchenko, *Nat. Nanotechnol.*, 2013, **8**, 100–103.
6 B. Hunt, J. D. Sanchez-Yamagishi, A. F. Young, M. Yankowitz, B. J. LeRoy, K. Watanabe, T. Taniguchi, P. Moon, M. Koshino, P. Jarillo-Herrero and R. C. Ashoori, *Science*, 2013, **340**, 1427–1430.
7 L. Liu, J. Park, D. A. Siegel, K. F. McCarty, K. W. Clark, W. Deng, L. Basile, J. C. Idrobo, A. P. Li and G. Gu, *Science*, 2014, **343**, 163–167.

8 K. S. Novoselov, A. Mishchenko, A. Carvalho and A. H. Castro Neto, *Science*, 2016, **353**, aac9439.
9 Y. Gong, J. Lin, X. Wang, G. Shi, S. Lei, Z. Lin, X. Zou, G. Ye, R. Vajtai, B. I. Yakobson, H. Terrones, M. Terrones, B. K. Tay, J. Lou, S. T. Pantelides, Z. Liu, W. Zhou and P. M. Ajayan, *Nat. Mater.*, 2014, **13**, 1135–1142.
10 C. M. Huang, S. F. Wu, A. M. Sanchez, J. J. P. Peters, R. Beanland, J. S. Ross, P. Rivera, W. Yao, D. H. Cobden and X. D. Xu, *Nat. Mater.*, 2014, **13**, 1096–1101.
11 X. P. Hong, J. Kim, S. F. Shi, Y. Zhang, C. H. Jin, Y. H. Sun, S. Tongay, J. Q. Wu, Y. F. Zhang and F. Wang, *Nat. Nanotechnol.*, 2014, **9**, 682–686.
12 M. Y. Li, Y. Shi, C. C. Cheng, L. S. Lu, Y. C. Lin, H. L. Tang, M. L. Tsai, C. W. Chu, K. H. Wei, J. H. He, W. H. Chang, K. Suenaga and L. J. Li, *Science*, 2015, **349**, 524–528.
13 Ç. Ö. Girit, J. C. Meyer, R. Erni, M. D. Rossell, C. Kisielowski, L. Yang, C. H. Park, M. F. Crommie, M. L. Cohen, S. G. Louie and A. Zettl, *Science*, 2009, **323**, 1075–1078.
14 T. Susi, J. Kotakoski, D. Kepaptsoglou, C. Mangler, T. C. Lovejoy, O. L. Krivanek, R. Zan, U. Bangert, P. Ayala, J. C. Meyer and Q. Ramasse, *Phys. Rev. Lett.*, 2014, **113**, 115501.
15 Z. Yang, L. Yin, J. Lee, W. Ren, H. M. Cheng, H. Ye, S. T. Pantelides, S. J. Pennycook and M. F. Chisholm, *Angew. Chem., Int. Ed.*, 2014, **53**, 1–6.
16 A. Azizi, X. Zou, P. Ercius, Z. Zhang, A. L. Elias, N. Perea-Lopez, G. Stone, M. Terrones, B. I. Yakobson and N. Alem, *Nat. Commun.*, 2014, **5**, 4867.
17 X. Liu, T. Xu, X. Wu, Z. Zhang, J. Yu, H. Qiu, J. H. Hong, C. H. Jin, J. X. Li, X. R. Wang, L. T. Sun and W. Guo, *Nat. Commun.*, 2013, **4**, 1776.
18 J. Lin, O. Cretu, W. Zhou, K. Suenaga, D. Prasai, K. I. Bolotin, N. T. Cuong, M. Otani, S. Okada, A. R. Lupini, J. C. Idrobo, D. Caudel, A. Burger, N. J. Ghimire, J. Yan, D. G. Mandrus, S. J. Pennycook and S. T. Pantelides, *Nat. Nanotechnol.*, 2014, **9**, 436–442.
19 Y. C. Lin, D. O. Dumcencon, Y. S. Huang and K. Suenaga, *Nat. Nanotechnol.*, 2014, **9**, 391–396.
20 D. Yang, S. J. Sandoval, W. M. R. Divigalpitiya, J. C. Irwin and R. F. Frindt, *Phys. Rev. B: Condens. Matter*, 1991, **43**, 12053–12056.
21 C. Xu, L. Wang, Z. Liu, L. Chen, J. Guo, N. Kang, X. L. Ma, H. M. Cheng and W. Ren, *Nat. Mater.*, 2015, **14**, 1135–1141.
22 Z. Liu, C. Xu, N. Kang, L. Wang, Y. Jiang, J. Du, Y. Liu, X. L. Ma, H. M. Cheng and W. Ren, *Nano Lett.*, 2016, **16**, 4243–4250.
23 L. Wang, C. Xu, Z. Liu, L. Chen, X. Ma, H. M. Cheng, W. Ren and N. Kang, *ACS Nano*, 2016, **10**, 4504–4510.
24 M. Naguib, V. N. Mochalin, M. W. Barsoum and Y. Gogotsi, *Adv. Mater.*, 2014, **26**, 992–1005.
25 M. R. Lukatskaya, O. Mashtalir, C. E. Ren, Y. Dall'Agnese, P. Rozier, P. L. Taberna, M. Naguib, P. Simon, M. W. Barsoum and Y. Gogotsi, *Science*, 2013, **341**, 1502–1505.
26 M. Ghidiu, M. R. Lukatskaya, M. Q. Zhao, Y. Gogotsi and M. W. Barsoum, *Nature*, 2014, **516**, 78–81.
27 B. Anasori, M. R. Lukatskaya and Y. Gogotsi, *Nat. Rev. Mater.*, 2017, **2**, 16098.
28 E. Parthé and V. Sadagopan, *Acta Crystallogr.*, 1963, **16**, 202–205.
29 T. Y. Velikanova, V. Z. Kublii and B. V. Khaenko, *Sov. Powder Metall. Met. Ceram.*, 1988, **27**, 891–896.
30 L. E. Toth, *Transition Metal Carbides and Nitrides*, Academic Press, 1971.
31 J. R. Politi, F. Vines, J. A. Rodriguez and F. Illas, *Phys. Chem. Chem. Phys.*, 2013, **15**, 12617–12625.
32 N. Morton, B. W. James, G. H. Wostenholm, D. G. Pomfret, M. R. Davies and J. L. Dykins, *J. Less-Common Met.*, 1971, **25**, 97–106.
33 W. Zheng, T. P. Cotter, P. Kaghazchi, T. Jacob, B. Frank, K. Schlichte, W. Zhang, D. S. Su, F. Schüth and R. Schlögl, *J. Am. Chem. Soc.*, 2013, **135**, 3458–3464.
34 K. Z. Qi, G. C. Wang and W. J. Zheng, *Surf. Sci.*, 2013, **614**, 53–63.
35 L. F. Chibotaru, A. Ceulemans, V. Bruyndoncx and V. V. Moshchalkov, *Phys. Rev. Lett.*, 2001, **86**, 1323–1326.
36 A. Kanda, B. J. Baelus, F. M. Peeters, K. Kadowaki and Y. Ootuka, *Phys. Rev. Lett.*, 2004, **93**, 257002.
37 H. Lin, Z. Shi, S. He, X. Yu, S. Wang, Q. Gao and Y. Tang, *Chem. Sci.*, 2016, **7**, 3399–3405.
38 H. Lin, W. Zhang, Z. Shi, M. Che, X. Yu, Y. Tang and Q. Gao, *ChemSusChem*, 2017, DOI: 10.1002/cssc.201700207.
39 B. Lonnberg, *J. Less-Common Met.*, 1986, **120**, 135–146.
40 A. N. Christensen, *Acta Chem., Scand. Ser. A*, 1977, **31**, 509–511.
41 X. W. Du, M. Takeguchi, M. Tanaka and K. Furuya, *Appl. Phys. Lett.*, 2003, **82**, 1108–1110.
42 A. Zobelli, A. Gloter, C. P. Ewels, G. Seifert and C. Colliex, *Phys. Rev. B: Condens. Matter*, 2007, **75**, 245402.